Reference to published article:
Schoepfer, V.A, & Lindsay, M.B.J. (2022). Repartitioning of co-precipitated Mo(VI) during Fe(II) and S(-II) driven ferrihydrite transformation. *Chemical Geology*, 610. https://doi.org/10.1016/j.chemgeo.2022.121075

Repartitioning of co-precipitated Mo(VI) during Fe(II) and S(-II) driven ferrihydrite transformation

Valerie A. Schoepfer* and Matthew B.J. Lindsay

Department of Geological Sciences, University of Saskatchewan,

114 Science Place, Saskatoon, SK, S7N 5E2, Canada

* Corresponding author: Tel: +1 306 966 5720; Fax: +1 306 966 8593.

E-mail addresses: valerie.schoepfer@usask.ca (V.A. Schoepfer); matt.lindsay@usask.ca (M.B.J. Lindsay)

Keywords: Mo(VI) reduction; ferrihydrite; sidwillite; kamiokite; ferruginous; sulfidic

Highlights:

- Fe(II) and S(-II) driven Mo repartitioning follow similar reaction pathways
- Mo is sequestered by discrete Mo minerals and neo-Fe(III) (oxyhydr)oxides
- Mo-S bonding absent in Mo K-edge EXAFS modeling
- Abundance of ferrihydrite more important for pathway progress than reductant type

ABSTRACT.

Molybdenum is an essential element for most biological systems. Biosynthesis of Mo-enzymes that support global biogeochemical cycles of N, C, and S depends upon bioavailable molybdate (MoO_4^{2-}). Interactions with Fe(III) (oxyhydr)oxides can limit Mo bioavailability in aerobic environments, while redox-driven mineral transformations can enhance Mo sequestration. Here, we examine Mo repartitioning during Fe(II) and S(-II) driven ferrihydrite transformation under anaerobic conditions. We reacted Mo(VI) co-precipitated 2-line ferrihydrite with $Fe(II)_{(aq)}$ or $S(-II)_{(aq)}$ and monitored geochemical and mineralogical changes over time. Inductively coupled plasma–mass spectrometry (ICP–MS) and synchrotron powder X-ray diffraction (XRD) results revealed rapid $Fe(II)_{(aq)}$ and $S(-II)_{(aq)}$ uptake and limited Mo release during extensive ferrihydrite transformation to goethite [α-FeOOH] and lepidocrocite [γ-FeOOH] in the Fe(II) and S(-II) experiments. Transmission electron microscopy–selected area electron diffraction (TEM-SAED), coupled with Mo L_{III}-edge and K-edge X-ray absorption near edge structure (XANES) spectroscopy, revealed partial Mo(VI) reduction and precipitation of kamiokite [$Fe_2Mo^{IV}_3O_8$] and sidwillite [$Mo^{VI}O_3{\cdot}2H_2O$] in both experiments. Extended X-ray absorption fine structure (EXAFS) spectroscopy at the Mo K-edge revealed Mo-O, Mo-Fe and Mo-Mo bonding consistent with kamiokite precipitation in both Fe(II) and S(-II) experiments, and the absence of Mo-S bonding in the S(-II) experiments. Similar Mo(VI) repartitioning pathways during Fe(II) and S(-II) driven ferrihydrite transformation suggests that: (i) Fe(II) served as the electron donor for ferrihydrite transformation in both experiments, with $Fe(II)_{(aq)}$ likely produced *in situ* via ferrihydrite sulfidation in the S(-II) experiments; and (ii) co-precipitation inhibited Mo release and limited subsequent interactions $S(-II)_{(aq)}$ during ferrihydrite transformation. Overall, our findings indicate that initial association with FeOx phases can strongly influence Mo sequestration pathways in anaerobic environments.

1. INTRODUCTION

Molybdenum is an essential element for life on Earth. Aqueous molybdate (MoO_4^{2-}) uptake enables biosynthesis of Mo enzymes that support diverse metabolic processes in plants, animals, and microbes (Gupta and Lipsett, 1981; Kaiser et al., 2005; Mendel and Kruse, 2012). These enzymes facilitate the global biogeochemical N, C and S cycles that have influenced biological and environmental coevolution over geologic time (Maia et al., 2017; Schwarz et al., 2009). Aqueous MoO_4^{2-} concentrations and the repartitioning of Mo between solid and aqueous phases are controlled by pH- and redox-dependent aqueous speciation, mineral interactions, and organic matter complexation (Goldberg et al., 1998; Helz and Vorlicek, 2019; Smedley and Kinniburgh, 2017). Past research into geochemical controls on MoO_4^{2-} mobility and bioavailability in aerobic environments show that adsorption to Mn(IV)oxides (Scholz et al., 2013; Xu et al., 2013) and Fe(III) (oxyhydr)oxides (FeOx) can decrease Mo(VI) availability (Arai, 2010; Das et al., 2016; Essilfie-Dughan et al., 2011; Görn et al., 2021; Gustafsson, 2003; Skierszkan et al., 2019). Studies focused on anaerobic environments indicate that Mo(VI) release from FeOx can occur under iron-reducing conditions, while formation of aqueous thiomolybdates ($Mo^{VI}O_xS_{4-x}^{2-}$) and sulfide phases (e.g., pyrite [FeS_2], mackinawite [FeS]) can enhance aqueous Mo sequestration under sulfate-reducing conditions (Bolanz et al., 2017; Bostick et al., 2003; Fox and Doner, 2003; Gomez et al., 2013; Hutchings et al., 2020; Robertson et al., 2019; Smedley et al., 2014; Wang et al., 2011; Xu et al., 2006). Few studies have considered how redox transitions, including shifts from oxic to anoxic conditions and oscillations between these conditions, influence Mo sequestration (Chappaz et al., 2008; Schoepfer et al., 2021, 2020).

Molybdate can accumulate in the neutral to alkaline pore waters of soils and sediments under aerobic conditions (Chappaz et al., 2008; Glass et al., 2013), where cellular MoO_4^{2-} uptake is favored (Demtröder et al., 2019; Kaiser et al., 2005). Conversely, complexation with organic matter and adsorption onto FeOx phases in acidic environments can limit Mo(VI) bioavailability (Marks et al., 2015; Wichard et al., 2009). For example, Mo complexation with FeOx and organic matter have corresponded to dampened N cycling and reduced plant productivity in aquatic, tropical, and temperate ecosystems (Barron et al., 2009; Glass et al., 2012; Perakis et al., 2017; Rousk et al., 2017; Williams, 1956; Winbourne et al., 2017; Wurzburger et al., 2012). Consequently, N cycling, the production of biologically available NH_3, and resulting plant productivity are dependent upon available Mo(VI). Iron is among the least abundant dissolved metals in the oceans due to the low solubility of FeOx phases at pH > 5 (Hunter and Boyd, 2007; Liu and Millero, 2002). Ferrihydrite is poorly crystalline FeOx phase with a large reactive surface area that is ubiquitous in oxic waters, soils and sediments, where co-precipitation, adsorption, and reduction reactions influence the mobility and bioavailability of Mo(VI) and other elements (Jambor and Dutrizac, 1998; Schultz et al., 1987).

Although ferrihydrite is an effective sink for Mo(VI) and other anions, redox transitions can promote transformation of metastable FeOx phases (Gomez et al., 2013; Han et al., 2019; Kocar et al., 2010; Tomaszewski et al., 2016; Usman et al., 2012). For example, adsorption of $Fe(II)_{(aq)}$ onto the ferrihydrite surface can promote recrystallization to goethite [α-FeOOH] and lepidocrocite [γ-FeOOH] *via* the electron transfer-atom exchange (ET-AE) reaction (Boland et al., 2014; Hansel et al., 2005). Repartitioning of associated Mo(VI) during Fe(II) driven ferrihydrite transformation can include structural incorporation into neoformed FeOx phases and precipitation of discrete Fe(III)-Mo(VI) phases (Schoepfer et al., 2021, 2020). Despite the

importance of sulfidic conditions for Mo sequestration, repartitioning of associated Mo(VI) during S(-II)-driven ferrihydrite transformation is poorly understood.

Molybdenum is a redox active transition metal, yet understanding of Mo(VI) reduction mechanisms in anaerobic environments remains incomplete (Smedley and Kinniburgh, 2017; Swedo and Enemark, 1979). Previous studies have reported the co-occurrence of Mo(IV) and Mo(VI) in sulfidic sediments and sedimentary rocks where Mo-S association is commonly observed (Ardakani et al., 2016; Chappaz et al., 2008; Dahl et al., 2017, 2013; Dahl and Wirth, 2017; Tessin et al., 2018). These findings are consistent with the formation of aqueous thiomolybdates and $FeMo^{VI}S_{4(s)}$, which are thought to precede Mo(VI) reduction by reduced S species (Helz et al., 2011, 2004; Helz and Vorlicek, 2019; Vorlicek et al., 2018, 2004). Bolanz et al. (2017) observed Mo(VI) reduction coupled with $Fe(II)_{(aq)}$ oxidation during microbial reduction of akaganeite [β-FeOOH] in the absence of reduced S compounds. Sulfidation of FeOx phases involves oxidation of S(-II) to elemental S [S_8] coupled with the reduction of structural Fe(III) to Fe(II) (Poulton et al., 2004). The formation of elemental S limits S(-II) availability, while Fe(II) can promote FeOx transformation *via* the ET-AE reaction (Boland et al., 2014). These previous findings suggest sulfidation of Mo(VI)-bearing FeOx phases likely promote complex reactions with implications for Mo sequestration.

In this study, we test the hypothesis that repartitioning of co-precipitated Mo among the aqueous and solid phases follows similar pathways during Fe(II)- and S(-II)-driven ferrihydrite transformation. We conducted laboratory batch experiments at pH 7.5 with suspensions of 2-line ferrihydrite synthesized with and without co-precipitated Mo(VI). We initiated transformation by introducing $Fe(II)_{(aq)}$ or $S(-II)_{(aq)}$, and monitored pH and dissolved Mo, Fe, and S(-II) concentrations over the 28-d reaction period. Synchrotron-based powder X-ray Diffraction

(XRD) and Transmission Electron Microscopy-Selected Area Electron Diffraction (TEM-SAED) analysis of reacted solids supported our identification of reaction products over time. We used X-ray absorption spectroscopy (XAS) at the Mo L_{III}-edge and Mo K-edge to probe associated changes in oxidation states, coordination, and bonding. Our results offer new insight into Mo sequestration mechanisms and pathways in the environment.

2. MATERIALS AND METHODS

2.1. Ferrihydrite synthesis

We followed the rapid titration method of Schwertmann and Cornell (1991) to synthesize 2-line ferrihydrite (Fh) and 2-line ferrihydrite co-precipitated with 25 μmol Mo(VI) g^{-1} (Fh-Mo). Briefly, we titrated 500 mL of a 0.2 M $Fe(NO_3)_3$ solution to pH 7.5 using approximately 300 mL of a 1 M KOH solution over ~30 minutes to synthesize approximately 25 g equivalent dry weight. During Fe-Mo synthesis, we added 0.09 g $Na_2MoO_4{\cdot}2H_2O$ to a small amount of KOH and added to the ferric nitrate solution to prevent ferric molybdate [$Fe_2(MoO_4)_3$] precipitation. We used high purity reagents (>99.9 %) and ultrapure water (>18.2 MΩ·cm) during synthesis.

We poured aliquots of the resulting suspensions into 50 mL centrifuge tubes. After centrifuging at 3000 rpm for 5 minutes, we decanted the supernatant, added 40 mL of ultrapure water and thoroughly mixed the suspension using a vortex stirrer. We repeated this process three times to remove residual salts before removing excess water by vacuum filtration. We stored the wet solids in a refrigerator at +4°C for up to 2 weeks before initiating the experiments. Powder XRD confirmed that both the Fh and Fh-Mo synthesis methods yielded 2-line ferrihydrite, while Mo K-edge extended X-ray absorption fine structure (EXAFS) spectroscopy verified structural incorporation of tetrahedrally-coordinated Mo(VI) during Fe-Mo synthesis.

2.2. Batch experiments

After weighing 0.3 g ± 0.02 g (equivalent dry weight) of Fh or Fh-Mo into 125 mL amber glass serum bottles, we transferred the bottles to an anoxic chamber (< 5 vol. % $H_{2(g)}$, balance $N_{2(g)}$). We prepared 54 individual bottles for each of the Fh and Fh-Mo solids to facilitate triplicate destructive sampling of control [$(Fh)_0$, $(Fh\text{-}Mo)_0$], Fe(II) [$(Fh)_{Fe}$, $(Fh\text{-}Mo)_{Fe}$], and S(-II) [$(Fh)_S$, $(Fh\text{-}Mo)_S$] experiments after 1, 3, 7, 14, 21, and 28 d. After 24 h of equilibration with the anoxic atmosphere, we added 100 mL of a $N_{2(g)}$-purged 50 mM NaCl electrolyte solution containing 50 mM MOPS buffer adjusted to pH 7.5 using 0.1 M KOH to each bottle.

We prepared 0.2 M $FeCl_2{\cdot}4H_2O$ and 0.2 M $Na_2S{\cdot}9H_2O$ stock solutions in $N_{2(g)}$-purged ultrapure water in the anoxic chamber. We then pipetted 1 mL of each stock solution into separate serum bottles containing Fh or Fh-Mo suspensions to achieve initial concentrations of 2.0 mM $Fe(II)_{(aq)}$ or $S(-II)_{(aq)}$. After initiating the experiments, we capped and crimp sealed the amber serum bottles before removing them from the chamber and continuously mixing the suspensions on a shaker table (20 rpm) until sampling. After 14 and 21 d, we added an additional 1 mL of the 0.2 M $Na_2S{\cdot}9H_2O$ stock solution as S(-II) concentrations had declined to < 25 μM.

2.3. Sample collection and analysis

We selected three bottles from each experiment and transferred them into the anoxic chamber for sampling after 1, 3, 7, 14, 21, and 28 d. After opening the bottles, we separated the aqueous and solid-phase by vacuum filtration using 0.45 μm polyethersulfone (PES) filter membranes (Pall Corporation) and acid-washed polysulfone filtration units (Nalgene, Thermo Scientific, USA). We immediately measured filtrate pH and Eh inside the anoxic chamber. We used a pH electrode (Orion 8156BNUWP ROSS Ultra, Thermo Scientific,USA) calibrated to

NIST traceable pH 4, 7, and 10 buffer solutions and assessed the redox electrode (Orion 9678BNWP, Thermo Scientific, USA) performance using ZoBell's solution and Light's solution.

We used the Ferrozine and methylene blue methods for spectrophotometric (Genesys 150 UV visible spectrophotometer, Thermo Scientific, USA) quantification of $Fe(II)_{(aq)}$ and $Fe_{(T)}$ concentrations as well as $S(-II)_{(aq)}$ concentrations (Lindsay and Baedecker, 1988; Viollier et al., 2000). The detection limit for both Fe and S(-II) was 2.5 μM. Using all plastic syringes (Norm-Ject, Henke-Sass Wolf, GmbH, Germany), we passed the remaining filtrate through 0.22 μm PES filters (Minisart, Sartorius AG, Germany) into two 15 mL high-density polyethylene (HDPE) bottles and acidified to pH < 2 with trace-metal grade HNO_3 (Optima, Fisher Chemical, USA). We quantified Mo using a triple quadrupole inductively coupled plasma-mass spectrometer (ICP-MS; iCAP TQe, Thermo Scientific, Germany), where the detection limit was 0.03 μM. Values for all aqueous parameters in the three replicate bottles for each experiment were averaged and one standard deviation of the mean is reported.

We transferred the vacuum filtered solid-phase samples into 5 mL centrifuge tubes. We capped and sealed the tubes, removed them from the anoxic chamber, and immediately submerged them in liquid N_2, and stored the flash frozen samples at -20° C until analysis. During experimental setup, we collected and preserved samples of the initial Fh and Fh-Mo solids following the same methods used for the reacted experimental samples.

2.4. X-ray diffraction

Synchrotron based powder XRD was performed on beamline 08-B1-1 (CMCF-BM) at the Canadian Light Source (CLS) to identify dominant mineral phases present in initial and reacted solids. After freeze drying these solids at -50°C for 24 h, we loaded ~10 mg into 0.5 mm inner diameter polyimide (Kapton) capillary tubes that we then sealed with ethyl cyanoacrylate

adhesive. These samples were prepared in the anoxic chamber, placed in a vacuum desiccator, and stored at -20 °C until analysis. Capillary tubes were mounted on the goniometer and continuously rotated during the 60 second exposure to the 18 keV (λ = 0.6888 Å) incident beam with a 200 μm aperture at a detector distance of 350 mm. We collected four two-dimensional diffraction patterns for each sample using a high resolution back-illuminated charge-coupled device (CCD) area detector (Rayonix MX300-HE, Rayonix L.L.C., USA). We processed each sample in GSAS-II using a lanthanum hexaboride standard, where between 2-4 images were binned to obtain 20,000 to 35,000 counts on the largest reflections (Toby and Von Dreele, 2013). All datasets were integrated between 2 and 39° 2θ in 0.01° steps for a total of 3700 points and detector glitches were removed. We conducted phase identification and performed semi-quantitative Rietveld Refinement using PANalytical X'Pert HighScore Plus version 3.0 (PANalytical B.V., The Netherlands).

2.5. Transmission electron microscopy

We examined samples collected after 1, 14, and 28 d using TEM-SAED (Hitachi High-Technologies Corp, Japan) to provide insight into nano-scale transformations. Freeze-dried samples were prepared for analysis by suspension in 100% ethanol and dispersion onto C-coated Cu grids, which were allowed to air dry. We operated the TEM at an accelerating voltage of 100 kV using a 1 μm spot size at up to $10^{5.3}$ times magnification. We extracted d-spacings from SAED images using the TEM toolbar in Fiji ImageJ (Schindelin et al., 2012) and compared results to known d-spaces for Fe, S, and Mo minerals. We used a d-spacing tolerance of ± 5% to account for error in manually drawing diffraction rings. We considered crystal morphology, d-spacings, and experimental conditions to support phase identification.

2.6. X-ray absorption spectroscopy

2.6.1. Mo L_{III}-edge

We collected Mo L_{III}-edge X-ray absorption near-edge structure (XANES) spectra to examine oxidation states and coordination environments. In the anoxic chamber, we spread powdered solids onto double-sided C tape, which was adhered to a Cu plate. We stored the plate in a vacuum desiccator within the anoxic chamber for up to 48 h until analysis. The XANES spectra were collected using the solid-state endstation on the SXRMB beamline (06B1-1) at the CLS. We used a dual Si(111) crystal monochromator with an energy resolution of 1×10^{-4} eV for energy selection and a beam spot size of ~1 mm × 4 mm. We measured fluorescence yield under high vacuum (~ 5×10^{-8} torr) using a 7-element Si drift detector (RaySpec, England). Duplicate Mo L_{III}-edge spectra were obtained using 2 eV steps in the pre-edge region (i.e., 2490–2515 eV), 0.15 eV steps over the XANES region (i.e., 2515–2545 eV), and 0.75 eV in the post-edge region (i.e., 2545–2650 eV). We performed data reduction and analysis using the program ATHENA in the Demeter package (Ravel and Newville, 2005).

2.6.2. Mo K-edge

We collected Mo K-edge XAS spectra across the EXAFS regions to further examine coordination environments and interatomic bond distances. We spread powdered samples and reference materials onto polyimide (Kapton) tape within the anoxic chamber and stored them within a vacuum desiccator at −20 °C until analysis. Spectra were collected at the CLS on the BioXAS-Main beamline (07ID-2M), which uses A LN_2-cooled pseudo-channel cut double Si (220) crystal monochromator and a Si mirror with an Rh coating for beam focusing. Prior to analysis, we transferred samples or reference materials into a LN_2-cooled cryostat (Oxford Instruments plc., UK) positioned between the I0 and I1 ionization chambers. We collected

fluorescence data using a 32-element Ge detector (CANBERRA Co., Canada) using Zr6-filters and Soller slits to enhance the signal-to-noise ratio. We adjusted slit openings to avoid fluorescence detector oversaturation during measurements on reference materials. Simultaneous collection of transmission spectra for a Mo(0) foil positioned downstream between the I1 and I2 ionization chambers supported energy calibration. The scan region ranged from -200 eV below the theoretical Mo K edge (20,000 eV) to k=15 $Å^{-1}$. We used 5 eV steps in the pre-edge region (i.e., 19800–19900 eV), 0.5 eV steps in the XANES region (i.e., 19900–21000 eV), and 0.05 k in the EXAFS region (i.e., 21000 eV to 15 $Å^{-1}$). We performed two or three replicate scans per sample and one or two scan per reference material.

We performed data reduction and analysis using the programs ATHENA and ARTEMIS in the Demeter package (Ravel and Newville, 2005). In the non-linear least squares EXAFS fitting, the amplitude reduction factor for all samples was first optimized for the initial Mo-bearing ferrihydrite, assuming an ideal first shell Mo-O coordination number of 4.0, and the resulting value of 0.82(5) was fixed for all subsequent samples. Initial path lengths (R) of Mo-O, Mo-Mo, and Mo-Fe were obtained from previous work for phases suggested from XRD and TEM-SAED measurements (Cesbron and Ginderow, 1985; Kanazawa and Sasaki, 1986; Schoepfer et al., 2021). These ideal values were used to calculate and refine coordination numbers (CNs) and interatomic distances for all samples. The fitting procedure was performed on the Fourier transform of the background subtracted, k^3 weighted, $\chi(k)$ spectrum of all samples from k = 3 – 10 A^{-1}. The fitting of multiple scattering paths was not attempted and the least complex model was chosen as the ideal fit when multiple models were plausible.

2.6.3. Reference materials

We collected Mo K-edge and L_{III}-edge spectra for nine reference materials including the initial Mo(VI) co-precipitated ferrihydrite, $Na_2Mo^{VI}O_4$ (99%, Sigma-Aldrich), $Mo^{VI}O_3$ (99.9995%, Sigma-Aldrich), $Mo^{IV}O_2$ (99%, Sigma-Aldrich), kamiokite [$Fe^{II}_2Mo^{IV}_3O_8$] (University of Arizona, Tuscon, USA), ferrimolybdite [$Fe^{III}_2(Mo^{VI}O_4)_3 \cdot nH_2O$] (Canadian Museum of Nature, Ottawa, Canada), bamfordite [$Fe^{III}Mo^{VI}_2O_6(OH)_3 \cdot H_2O$] (Museums Victoria, Melbourne, Australia), sidwillite [$Mo^{VI}O_3 \cdot 2H_2O$] (National Museum of Scotland, Edinburgh, Scotland), and molybdite [$Mo^{VI}O_3$] (National Museum of Scotland, Edinburgh, Scotland). In addition to these references, we obtained Mo L_{III}-edge spectra for Mo(0) metal (Freitas et al., 2021). Linear combination fitting of the Mo K-edge spectra was conducted from -20 eV to 30 eV surrounding E_0, but LCF was not conducted on the L_{III}-edge due to relatively noisy pre- and post-edge regions. However, the L_{III}-edge spectra were sufficiently resolved to extract E_0 and qualitative peak shapes.

2.7. Thermodynamic modelling

Thermodynamic modelling of aqueous chemistry was performed using PHREECi (Version 3.5.0-14000) and a modified version of the minteq.V4 database (Parkhurst and Appelo, 2013). These modifications include the addition of aqueous molybdate ($NaMoO_4^-$, $KMoO_4^-$) thiomolybdate (MoO_3S^{2-}, $MoO_2S_2^{2-}$, $MoOS_3^{2-}$, MoS_2^{2-}) species with associated constants summarized by Chappaz et al. (2008). Non-detect aqueous Mo concentrations were input as one-half of the method detection limit (0.0007 uM) and input values for Fe(II) were determined using the Ferrozine method.

3. RESULTS

3.1. Aqueous chemistry

Slight pH decreases and increases after 1 d were observed in the Fe(II) and S(-II) experiments, respectively. Subsequent variations were limited in the $(Fh)_0$ (7.4 σ = 0.02), $(Fh\text{-}Mo)_0$ (7.5 σ = 0.01), $(Fh)_{Fe}$ (7.2 σ = 0.01), and $(Fh\text{-}Mo)_{Fe}$ (7.3 σ = 0.01) experiments. Larger pH increases to between 8.0 and 8.2 were observed following additional S(-II)(aq) additions to the $(Fh)_S$ and $(Fh\text{-}Mo)_S$ experiments at 14 d and 21 d (Figure 1).

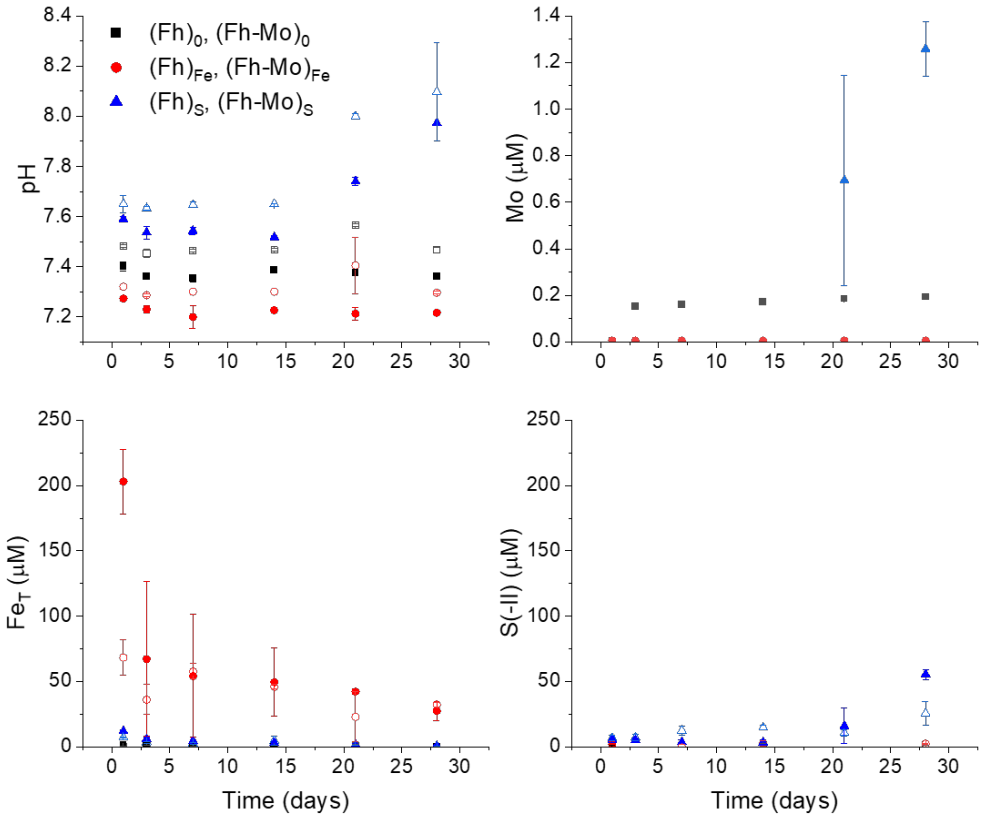

Figure 1. Mean aqueous pH, Mo, Fe_T, and S(-II) concentrations in the Fh-Mo experiments (filled symbols) and Fh experiments (open symbols) with error bars depicting one standard deviation from the mean.

Dissolved Fe_T was low in both the $(Fh\text{-}Mo)_0$ and $(Fh)_0$ experiments, with concentrations remaining < 1.5 μM throughout the 28 d experiment (Figure 1). In the $(Fh\text{-}Mo)_{Fe}$ experiments, Fe_T concentrations after 1 d were 203 μM (1 σ = 24.7 μM) and this value decreased rapidly to a low of 27 μM (1 σ = 7.3 μM) at 28 d. In contrast, the $(Fh)_{Fe}$ experiments exhibited much lower aqueous Fe_T concentrations, which decreased from 68.3 μM (1 σ = 13.8 μM) at 1 d to 23 μM (1 σ = 19.2 μM) at 21 d. Aqueous Fe_T concentrations in the $(Fh)_S$ and $(Fh\text{-}Mo)_S$ experiments were 12.0 μM (1 σ = 1.1 μM) and 7.2 μM (1 σ = 0.3 μM), respectively, after 1 d and decreased to < 0.8 μM after 28 d. Approximately 90 % of dissolved Fe_T occurred as $Fe(II)_{(aq)}$ in the Fe(II) and S(-II) experiments (Figure S1).

Concentrations of $S(-II)_{(aq)}$ were consistently < 3 μM in the $(Fh\text{-}Mo)_0$ and $(Fh\text{-}Mo)_{Fe}$ experiments, to which S(-II) was not added (Figure 1). For the $(Fh\text{-}Mo)_S$ experiments, $S(-II)_{(aq)}$ concentrations were 5.6 μM (1 σ = 0.7 μM) at 1 d and decreased to 3.3 μM (1 σ = 2.0 μM) at 14 d. Subsequent S(-II) additions after 14 d and 21 d sampling temporarily returned $S(-II)_{(aq)}$ concentrations to the 2 mM initial value. However, $S(-II)_{(aq)}$ concentrations in the $(Fh\text{-}Mo)_S$ experiment subsequently decreased to 16.0 μM (1 σ = 13.5 μM) after 21 d and to 55.5 μM (1 σ = 3.8 μM) after 28 d. Concentrations of $S(-II)_{(aq)}$ in the $(Fh)_S$ experiments were 6.8 μM (1 σ = 2.0 μM) after 1 d and 14.7 μM (1 σ = 1.5 μM) after 14 d. Following the 14 and 21 d S(-II) additions, $S(-II)_{(aq)}$ concentrations subsequently decreased to 10.5 μM (1 σ = 2.6 μM) after 21 d and to 25.5 μM (1 σ = 9.2 μM) after 28 d.

Molybdenum concentrations in the $(Fh\text{-}Mo)_0$ experiments remained below 0.31 μM throughout the 28 d experiment, while they remained below 0.01 μM for the 28 d of the $(Fh\text{-}Mo)_{Fe}$ experiments (Figure 1). Concentrations were below 0.05 μM during the first 14 d of the $(Fh\text{-}Mo)_S$ experiments, but subsequently increased to 0.69 μM (1 σ = 0.45 μM) and 1.26 μM (1 σ

= 0.12 μM) at 21 and 28 d, respectively. Thermodynamic modelling indicates that MoO_4^{2-} and $NaMoO_4^-$ consistently accounted for over 99 % of dissolved Mo in the $(Fh\text{-}Mo)_{Fe}$ experiments (Table S4). In the $(Fh\text{-}Mo)_S$ experiments, aqueous thiomolybdates consistently comprised < 9 % of dissolved Mo through 14 d (Table S5). Following S(-II) additions after 14 d and 21 d, the proportion of dissolved Mo associated with thiomolybdates increased to 14.0 % (1 σ = 12.3 %) and 26.3 % (1 σ = 1.4 %) at 21 and 28 d, respectively.

3.2. X-ray diffraction

Synchrotron powder XRD results indicate that 2-line ferrihydrite was the only phase present in the $(Fh\text{-}Mo)_0$ experiments (Figure 2). In contrast, a mixture of lepidocrocite [γ-FeOOH], goethite [α-FeOOH], and magnetite [Fe_3O_4] were detected after 1 d in the $(Fh\text{-}Mo)_{Fe}$ experiments. The abundance of lepidocrocite subsequently decreased relative to goethite and magnetite (Figure 3). In the $(Fh\text{-}Mo)_S$ experiments, goethite and lepidocrocite each accounted for ~50 % of reacted solids after 1 d. Subsequent decreases in the relative abundance of lepidocrocite to < 5 % after 7 d and to 0 % after 21 d generally corresponded to increases in the relative abundance of goethite (Figure 3). Minor elemental S [S_8] was also detected in the $(Fe\text{-}Mo)_S$ experiments, while magnetite and other phases were absent or below detection.

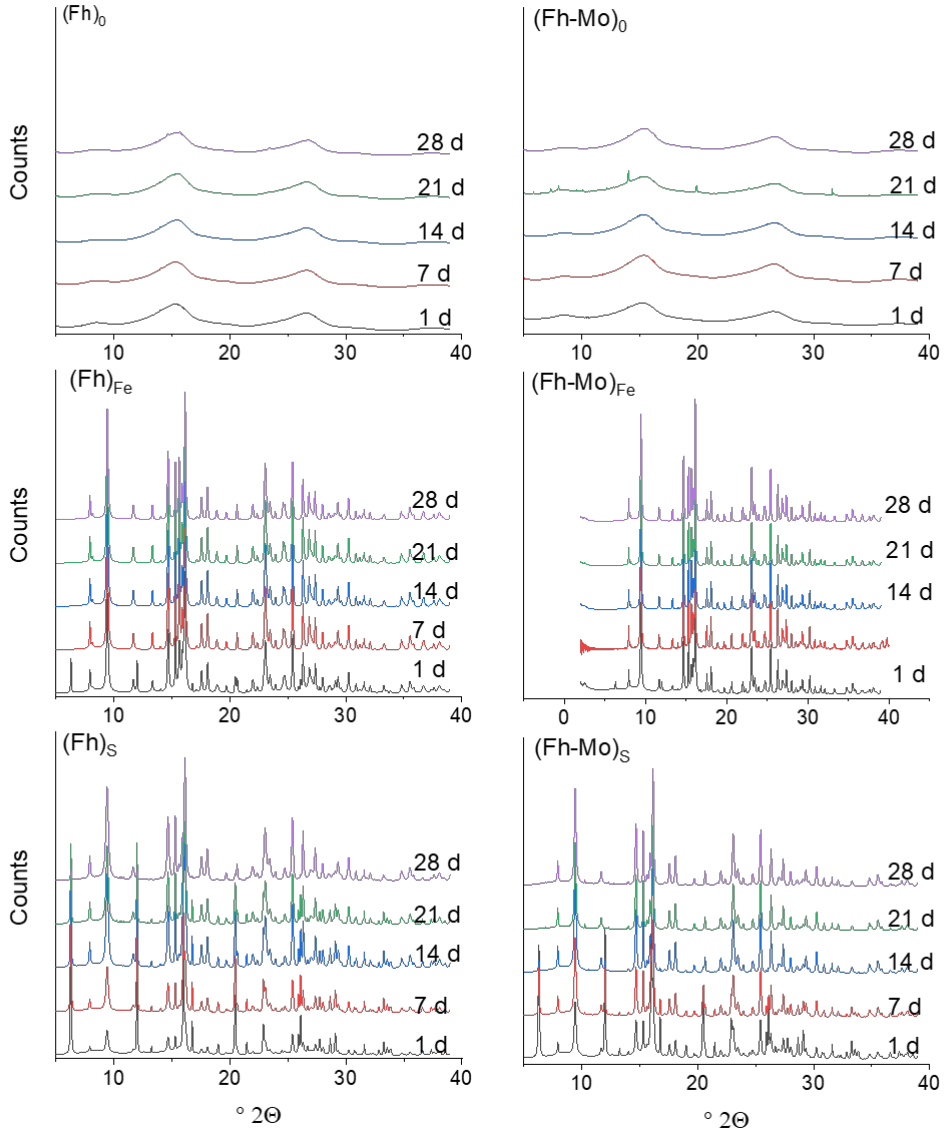

Figure 2. X-ray diffraction patterns for the (left) Mo-free and (right) Mo-containing experiments, depicting reductant-free controls (top), Fe(II) amended experiments (second row), S(-II) amended experiments (third row), and reference materials (bottom).

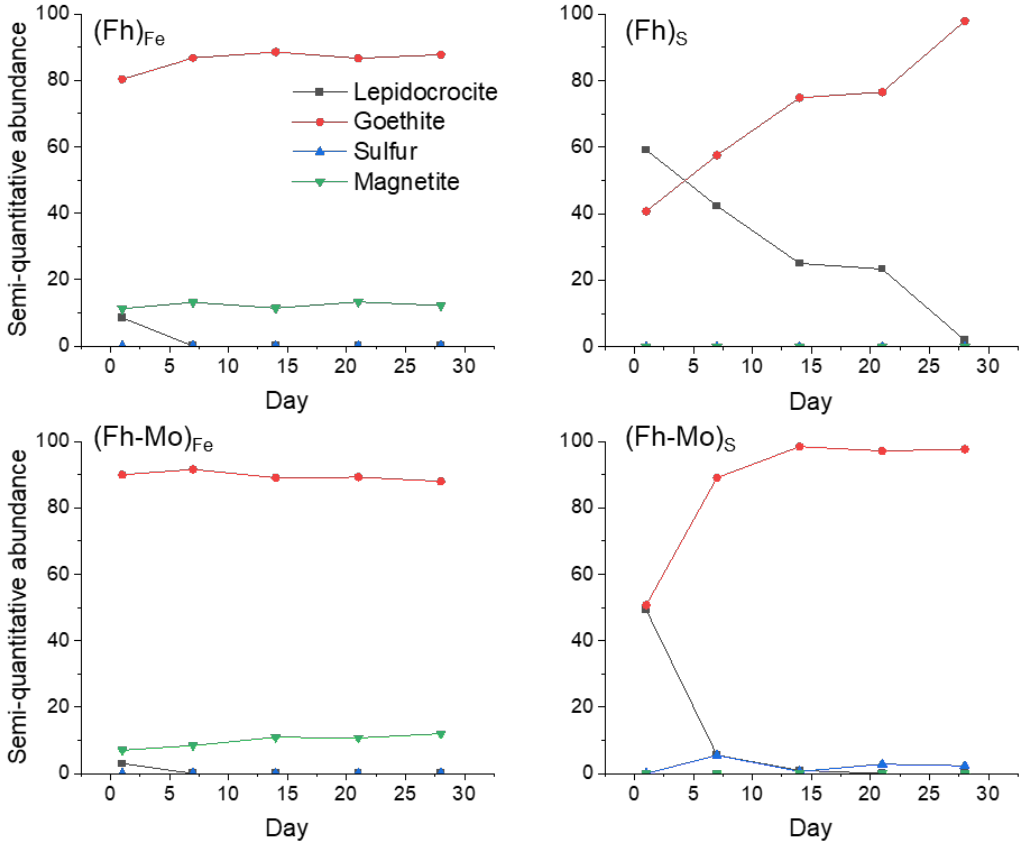

Figure 3. Semi-quantitative Rietveld Refinement for the $(Fh)_{Fe}$ experiments (top left), the $(Fh)_S$ experiments (top right), the $(Fh\text{-}Mo)_{Fe}$ experiments (bottom left) and $(Fh\text{-}Mo)_S$ experiments (bottom right).

The persistence of ferrihydrite in the $(Fh)_0$ experiment is contrasted by the formation of lepidocrocite, goethite, and magnetite in the $(Fh)_{Fe}$ experiment (Figure 3). Lepidocrocite and goethite were the only Fe phases detected in the $(Fh)_{Fe}$ experiment, with the relatively proportion of lepidocrocite decreasing relative to goethite over time (Figure 3). Minor peaks associated with mackinawite [FeS] suggest this phase formed in the $(Fh)_S$ experiments, while elemental S was detected after 21 and 28 d.

3.3. Transmission electron microscopy

Examination of initial Mo-bearing solids by TEM-SAED revealed poorly crystalline ferrihydrite clusters that produced diffuse diffraction patterns. Ferrihydrite persisted throughout the $(Fh\text{-}Mo)_0$ experiment, whereas highly structured crystallites appeared after 1 d in the $(Fh\text{-}Mo)_{Fe}$ experiment (Figure 4). These neoformed phases included ~1 μm wide tabular crystallites consistently identified by SAED as kamiokite, plus clusters of ~500 nm long lathe-like lepidocrocite and <250 nm diameter single and twinned goethite rods. Although molybdite was consistently detected in reacted samples from the $(Fh\text{-}Mo)_{Fe}$ experiment, the crystallites exhibit similar morphology to goethite and d-spacings are comparable to sidwillite. Sidwillite displays a slightly elongated hexagonal and tabular macro-morphology but its nano-scale particle size is unknown (Cesbron and Ginderow, 1985). Kamiokite crystallites were not observed at 14 or 28 d, when the majority of neoformed crystallites resembled goethite rods.

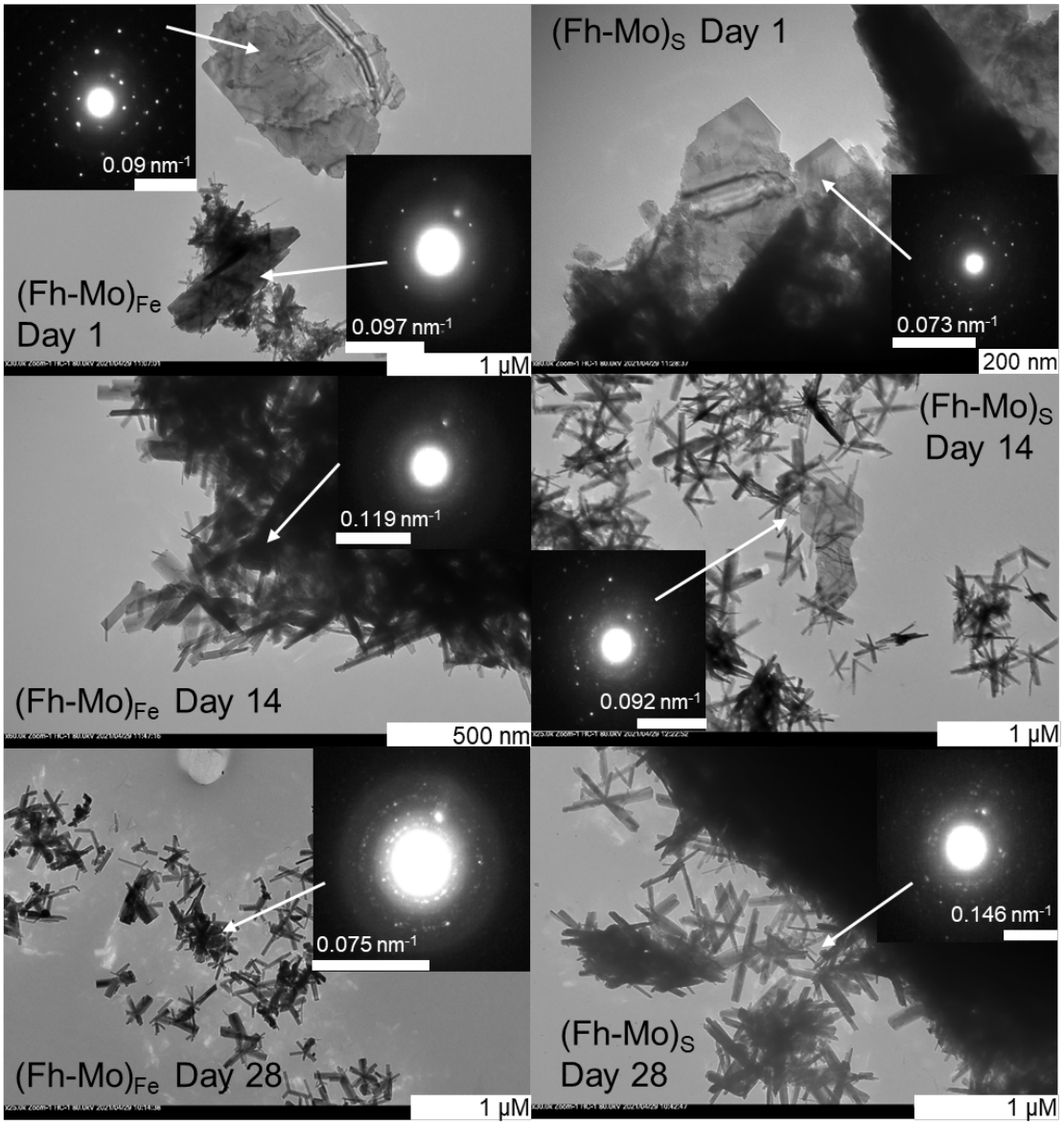

Figure 4. Transmission electron microscopy (TEM) images for the $(Fh\text{-}Mo)_{Fe}$ experiments (left) and the $(Fh\text{-}Mo)_S$ experiments (right) with inset selected area electron diffraction (SAED) patterns for the center of each image when not indicated by white arrows.

Reacted solids from the $(Fh\text{-}Mo)_S$ and $(Fh\text{-}Mo)_{Fe}$ experiments exhibited similar phases at 1 d, including tabular kamiokite crystallites, lathe-like lepidocrocite, and both single and twinned goethite rods (Figure 4). Both kamiokite and goethite were observed through 14 d in the (Fh-

$Mo)_S$ experiment, whereas single and twinned goethite rods dominated after 28 d. Molybdite and mackinawite were also identified throughout the 28 d $(Fh\text{-}Mo)_S$ experiment.

3.4. X-ray absorption spectroscopy

3.4.1. Mo L_{III}-edge XANES

The first-derivative E_0 positions was 2523.1 eV for both the initial and 28 d solids from the $(Fh\text{-}Mo)_0$ experiment. This value is consistent with the average E_0 positions of 2523.1 eV obtained for the Na_2MoO_4 and MoO_3 reference materials. The E_0 positions of 28 d reacted solids from the $(Fh\text{-}Mo)_{Fe}$ and $(Fh\text{-}Mo)_S$ experiments were 2522.1 eV and 2522.0 eV, respectively. These values are slightly higher than E_0 positions of 2520.9 eV and 2519.6 eV obtained for the MoO_2 reference material and Mo(0) foil, respectively. This slight decrease in E_0 positions are consistent with partial Mo(VI) reduction in the $(Fh\text{-}Mo)_{Fe}$ and $(Fh\text{-}Mo)_S$ experiments (Figure S3).

3.4.2. Mo K-edge EXAFS

Modeled K-edge EXAFS spectra for reacted solids from the $(Fe\text{-}Mo)_0$ experiment revealed limited change in local Mo coordination and bonding over time (Figure 5, Table S1). The principal Mo-O scattering path included 3.6–3.9 O atoms at positioned 1.73–1.75 Å from the central Mo atom.

Spectra obtained for solids from the $(Fh\text{-}Mo)_{Fe}$ experiments exhibited substantial differences from the control, but exhibited limited change from 1 d through 28 d (Figure 5, Table S2). Best fit EXAFS models included five scattering paths with distinct interatomic distances, including Mo-O paths at 1.82 Å ($Mo\text{-}O_1$) and 2.06 Å ($Mo\text{-}O_2$), Mo-Fe paths at 2.68 Å ($Mo\text{-}Fe_1$) and 3.58 Å ($Mo\text{-}Fe_2$), and an Mo-Mo path at 3.34 Å. Modeled coordination numbers for the Mo-

O paths ranged from 2.3 to 4.4, averaging 3.57 and 2.56 for Mo-O_1 and MoO_2, respectively. Models including these Mo-O interatomic distances required an R_{bkg} value around 0.7 and background spline fitting within the Artemis program, due to overlap between the background and first shell Fourier components. Coordination numbers ranged from 0.3 to 0.4 for Mo-Fe_1, from 0.9 to 1.5 for Mo-Fe_2, and from 1.1 to 1.4 for Mo-Mo. The interatomic distances for the Mo-Mo and Mo-Fe_2 paths were comparable to the Mo-Mo and Mo-Fe paths at 3.24 Å for kamiokite (Kanazawa and Sasaki, 1986; Ravel, 2001; Sasaki et al., 1985).

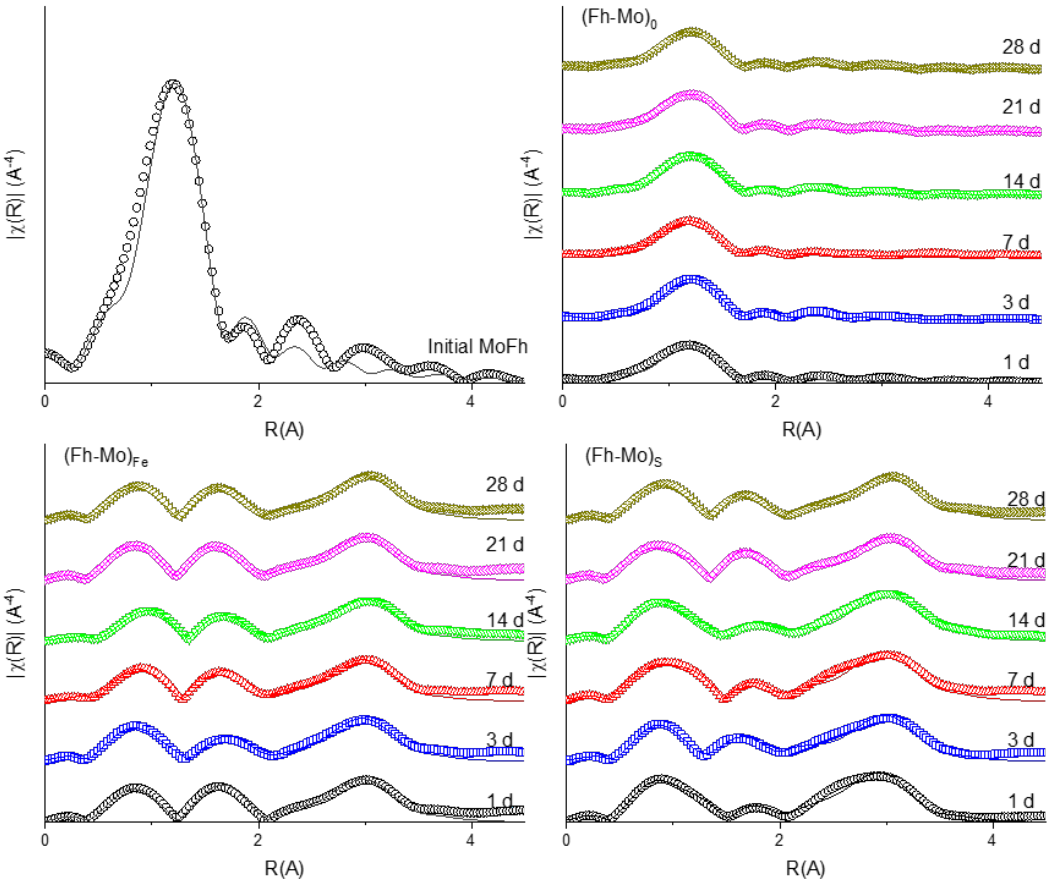

Figure 5. Mo K-edge extended X-ray absorption fine structure (EXAFS) spectra for the (Fh-Mo)$_0$, (Fh-Mo)$_{Fe}$, and (Fh-Mo)$_S$ experiments. Data are indicated by points while the fitted models

are indicated by a solid line. Fitting with multiple scattering paths was not attempted. All paths and fitting parameters used are in the supporting information.

Spectra for reacted solids from the $(Fe\text{-}Mo)_S$ and $(Fe\text{-}Mo)_{Fe}$ experiments were generally consistent (Figure 5, Table S3). Best fit EXAFS models included Mo-O paths at distances of 1.8 Å (Mo-O_1) and 2.06 Å (Mo-O_2) with coordination numbers averaging 4.6 and 2.0, respectively. These models required the same low R_{bkg} and background spline fitting requirement as the $(Fh\text{-}Mo)_{Fe}$ experiments. The average interatomic distances for the Mo-Mo and Mo-Fe_2 paths were 3.35 Å and 3.57 Å, respectively, which is slightly longer than that of kamiokite (Kanazawa and Sasaki, 1986; Ravel, 2001; Sasaki et al., 1985). These distances converged slightly over time, reaching 3.37 Å (Mo-Mo) and 3.54 Å (Mo-Fe_2) after 28 d. Coordination numbers ranged from 0.4 to 0.5 for the Mo-Fe_1 path, 1.0 to 1.5 for the Mo-Fe_2 path, and 1.4 to 1.7 for the Mo-Mo path. Best fit models did not include any Mo-S scattering paths.

4. DISCUSSION

4.1. Ferrihydrite transformation

Ferrihydrite persisted in the $(Fh)_0$ and $(Fh\text{-}Mo)_0$ experiments, without the addition of Fe(II) or S(-II) to promote transformation via the ET-AE reaction (Boland et al., 2014; Hansel et al., 2005; Liu et al., 2007). In contrast, crystalline secondary FeOx phases formed rapidly after the addition of Fe(II) and S(-II) to ferrihydrite synthesized with and without co-precipitated Mo(VI). This observation indicates that co-precipitated Mo(VI) did not influence ferrihydrite transformation pathways. The immediate precipitation of magnetite, goethite, and lepidocrocite corresponded to large decreases in $Fe(II)_{(aq)}$ concentrations in the Fe(II) experiments. These observations indicate that initial uptake produced Fe(II) surface loadings sufficient to drive rapid

ferrihydrite transformation (Boland et al., 2014; Hansel et al., 2005; Liu et al., 2007). Although magnetite was consistently detected, the relative abundance of this transformation product remained relatively constant during the experiment. The decreasing relative abundance of lepidocrocite at early time is attributed to ongoing recrystallization to goethite during continued reaction with Fe(II) (Hansel et al., 2005; Yan et al., 2016).

The initial formation of goethite and lepidocrocite in the S(-II) experiments is consistent with Fe(II) driven ferrihydrite transformation via the ET-AE reaction (Boland et al., 2014). However, rapid decreases in $S(-II)_{(aq)}$ concentrations also corresponded to the formation of relatively minor amounts of elemental S and FeS. The formation of elemental S is indicative of structural Fe(III) reduction to Fe(II) coupled with the oxidation of S(-II) to S(0) in a ferrihydrite sulfidation reaction, while the presence of both S(-II) and Fe(II) can promote FeS precipitation (Figure S4) (Hockmann et al., 2020; Kocar et al., 2010; Poulton et al., 2004; Zhang et al., 2019). The Fe(II) produced during sulfidation can also promote ferrihydrite transformation to more crystalline phases including lepidocrocite and goethite (ThomasArrigo et al., 2020). Consequently, our results suggest an indirect role for S(-II) where Fe(II) generated during ferrihydrite sulfidation promotes transformation to goethite and lepidocrocite.

Magnetite, which typically precipitates under higher Fe(II) surface loadings than goethite (Hansel et al., 2005), was not observed in the S(-II) experiments. This observation indicates that Fe(II) availability for ET-AE was limited in the S(-II) experiments compared to the Fe(II) experiments. Furthermore, the complete transformation of lepidocrocite to goethite took over 14 days in the S(-II) experiments and less than 7 days in the Fe(II) experiments. Lower Fe(II) availability in the S(-II) experiments may be due to the kinetics of ferrihydrite sulfidization, where the rate of Fe(II) production is dependent upon mineral surface area and crystallinity

(Poulton et al., 2004). Therefore, slower transformation rates observed in the S(-II) experiments are attributed to declining Fe(II) production coupled with ongoing formation of more ordered goethite (Poulton et al., 2004; Southall et al., 2018).

4.2. Molybdenum repartitioning

Limited Mo release was observed in the $(Fe\text{-}Mo)_0$ control, where > 99.5 % of co-precipitated tetrahedral Mo(VI) persisted throughout the experiment. Despite extensive ferrihydrite transformation, Mo release was also limited throughout the Fe(II) experiments and over the first 14 d of the S(-II) experiments. This observation is consistent with extensive Mo sequestration by initial transformation products, which included lepidocrocite and goethite. Previous studies likewise demonstrate that following initial Mo release, transformation products including lepidocrocite, goethite, and bamfordite [$FeMo^{VI}_2O_6(OH)_3 \cdot H_2O$] can sequester Mo(VI) during the Fe(II)-driven ET-AE reaction (Gomez et al., 2013; Schoepfer et al., 2021, 2020). Similarly, As(V) retention by neoformed goethite and magnetite has previously been reported during redox-induced transformation of As(V)-bearing FeOx phases (Kocar et al., 2006; Pedersen et al., 2006). Increasing dissolved Mo concentrations after 21 d and 28 d in the S(-II) experiments suggest that subsequent S(-II) additions promoted Mo release. These increases corresponded to a slight pH increase from 7.5 to 8.0 and sustained elemental S precipitation. Thermodynamic modelling indicates that aqueous thiomolybdate species accounted for a greater proportion of total dissolved Mo at 21 d and 28 d following supplemental S(-II) additions (Table S5). Coupled with the apparent absence of Mo-S bonding in our Mo K-edge EXAFS models, these results suggest S-bearing reaction products were not major drivers of Mo sequestration. Previous studies similarly show that mackinawite, greigite and elemental S exhibit limited capacity for As retention during ferrihydrite sulfidation compared to neoformed FeOx phases

(Burton et al., 2011; Huang et al., 2015; Kocar et al., 2010). Conversely, in the presence of ~9 mole % PO_4^{3-}, sulfidation effectively and disproportionately liberated PO_4^{3-} from ferrihydrite (Kraal et al., 2022). Helz et al. (2004) observed temporary Mo scavenging during FeS precipitation and subsequent release during further crystallization of FeS to greigite. These authors also noted that thiomolybdates were more effectively sequestered by FeS than MoO_4^{2-}, which accounted for a larger proportion of total dissolved Mo in our experiments (Table S5).

Best fit Mo K-edge EXAFS models indicates that octahedrally coordinated Mo dominated in all reacted solids from the Fe(II) and S(-II) experiments compared to the tetrahedrally coordinated Mo in the initial solids and reacted solids from the control experiment. This finding is consistent with previous results reported by Schoepfer et al. (2021). Nearly all of the co-precipitated Mo was retained in the solid phase throughout the 28 d Fe(II) and S(-II) experiments, with both discrete Mo minerals and FeOx phases contributing to Mo sequestration. In support, the modeled Mo-Fe interatomic distances of 2.7 and 3.5 Å generally correspond to established values of 2.8-2.9 Å and 3.5-3.6 Å for co-precipitated Mo within FeOx structures (Arai, 2010; Görn et al., 2021; Gustafsson and Tiberg, 2015; Kashiwabara et al., 2011; Skierszkan et al., 2019).

Despite extensive Mo retention, the small Mo K-edge XANES pre-edge feature and Mo L_{III}-edge XANES extracted E_0 values shows that retained octahedral Mo includes both Mo(VI) and Mo(IV). This finding is indicative of partial Mo(VI) reduction by $Fe(II)_{(aq)}$, with XAS and TEM-SAED observations also revealing the formation of discrete Mo minerals near the mineral-water interface. In particular, the Mo K-edge LCF results suggest the presence of sidwillite, kamiokite, and bamfordite, and the absence of tetrahedral Mo(VI) initially associated with ferrihydrite. The presence of these phases further support the paths modeled by Mo K-edge

EXAFS fitting. Although interatomic distances for modeled Mo-Fe_2 (3.5 Å) and Mo-Mo (3.35 Å) paths are similar to distorted and shared Mo and Fe shells for kamiokite, multiple paths associated with kamiokite, sidwillite, bamfordite, and octahedral Mo associated with FeOx phases could produce similar spectra.

Observations made with TEM-SAED, Mo L_{III}-edge XANES, and Mo K-edge EXAFS indicate that kamiokite was a substantial component of the solid phase Mo pool throughout the Fe(II) and S(-II) experiments (Endo et al., 1986; Kanazawa and Sasaki, 1986; Sasaki et al., 1985). For example, the proportion of Mo(IV) in the solid phase progressively increased throughout both 28 d experiments as indicated by the gradually decreasing E_0 position in the Mo L_{III} edge XANES (Figure S2), and supports the ongoing precipitation of Mo(IV)-bearing kamiokite over time. Furthermore, TEM-SAED analysis confirmed the presence of kamiokite in reacted solids from the Fe(II) and S(-II) experiments, which supported including of this Mo(IV) bearing phase in best fit Mo K-edge EXAFS models. Kamiokite precipitation occurs under S(-II) limited conditions, whereas molybdenite [MoS_2] precipitation is favored as S(-II) availability increases (Johan and Picot, 1986; Sasaki et al., 1985). Consequently, limited $S(-II)_{(aq)}$ concentrations in our experiments likely favored kamiokite precipitation.

Although Mo(IV)-bearing kamiokite represented a substantial component of Mo in reacted solids, both bamfordite and sidwillite were also detected in reacted solids from the Fe(II) and S(-II) experiments. The formation of these phases under low $Mo_{(aq)}$ and $Fe_{(aq)}$ concentrations suggests these reactions occurred at ferrihydrite surfaces. Bamfordite has recently been described as a product of ET-AE in Mo(VI)-containing ferrihydrite (Schoepfer et al., 2021), whereas sidwillite is thought to precipitate as an oxidation product of jordisite [amorphous $Mo^{IV}S_2{\cdot}nH_2O$] (Cesbron and Ginderow, 1985), which has been linked to the Fe-Mo-S colloids found in sulfidic

paleo-environmental sediments (Vorlicek et al., 2018). However, our Mo K-edge LCF and TEM-SAED results suggest that either sidwillite or molybdite formed in both the presence and absence of $S(-II)_{(aq)}$. Furthermore, reports of MoO_3 phases in sulfidic muds and sediments using XAS-based techniques are often attributed to an unknown, and possibly organically-bound octahedral Mo(VI) species rather than molybdite or sidwillite, as these phases are thought to rarely occur in nature (Ardakani et al., 2016; Tessin et al., 2018; Wagner et al., 2017). The short and relatively unique 1.68 Å Mo-O interatomic distance characteristic of the hydrated and distorted sidwillite was not explicitly observed in our best fit EXAFS modeling, although it was suggested in other, non-best fit EXAFS models, while other Mo-O paths found in sidwillite and molybdite were included in the best fit models. This result may relate to the relatively low abundance of MoO_3 phases in the reacted solids. However, inclusion of sidwillite in the LCF of most Mo K-edge XANES spectra suggests that the transformation of co-precipitated Mo(VI) may favor precipitation of MoO_3 phases in the absence of natural organic matter. This Mo-O bond at 1.68 Å has been reported in previous Mo K-edge EXAFS studies of sulfidic muds, which also infer relationships between the precipitation of MoO_3 phases and Mo-S bonding (Dahl et al., 2017, 2013; Helz et al., 1996). Consequently, our results are consistent with previous studies reporting precipitation of MoO_3 phases in the absence of $S(-II)_{(aq)}$ (Ardakani et al., 2016; Tessin et al., 2018; Wagner et al., 2017).

4.3. Relative roles of Fe and S

The apparent absence Mo-S bonding in the 28 d reacted solids form S(-II) experiments strongly indicates that $S(-II)_{(aq)}$ indirectly drives FeOx transformation and Mo repartitioning through $Fe(II)_{(aq)}$ production. The absence of Mo-S bonding further limits the possibility of substantial co-precipitated Mo in FeS or elemental S in our study, or alternatively, the precipitation of a black and amorphous Fe-Mo sulfide species (Helz et al., 2011, 1996). Thermodynamic modelling indicates that aqueous thiomolybdate species represented a minor component of total dissolved Mo in the S(-II) experiments (Table S5) and were absent in the Fe(II) experiments (Table S4). Previous studies show that thiomolybdates are effectively sequestered or transformed by mackinawite, pyrite, elemental S and other S phases (Bostick et al., 2003; Helz et al., 2004; Vorlicek et al., 2004; Yang et al., 2015). However, these reactions produce Mo-S bonding, which was absent in best fit Mo K-edge EXAFS models for reacted solids from the S(-II) experiments. Consequently, Fe(II)-driven processes dominate at early time, when the majority of Fh transformation and Mo repartitioning occurs, and may contrast, or perhaps precede the processes outlined by previous work, which suggest $S(-II)_{(aq)}$ will initiate the formation of aqueous thiomolybdate species, Fe-Mo-S precipitates, or molybdenite [$Mo^{IV}S_2$] (Dahl and Wirth, 2017; Erickson and Helz, 2000; Helz et al., 1996; Yang et al., 2015; Zheng et al., 2000). Therefore, Mo cycling in the presence of $S(-II)_{aq}$ may follow different pathways as dependent on dominant reduction chemistry.

The initial presence of co-precipitated Mo(VI) may also influence potential for Mo-S bonding during ferrihydrite sulfidation. Co-precipitation of anions with FeOx phases is environmentally common (Carlson et al., 2002; Chapman et al., 1983; Hudson-Edwards et al., 1999; Park et al., 2016), and can occur when Fe(II) rich waters become oxygenated in the

presence of anions. Co-precipitation limits anion mobilization and binding with other elements when compared to adsorption (Kraal et al., 2022; Schoepfer et al., 2021). However, past studies on Mo cycling in marine systems often assumes initial Mo(VI) adsorption onto FeOx phases, even when pH conditions would favor co-precipitation over adsorption (Chappaz et al., 2008; Dahl et al., 2011; Scholz et al., 2017, 2013). For example, Mo(VI) sorption to ferrihydrite at pH 8.5, which is consistent with seawater and an ionic strength of 10 mM is limited, with maximum adsorption of ~0.4 μmol Mo g^{-1} ferrihydrite (Gustafsson, 2003). Schoepfer et al. (2021) found that co-precipitation can incorporate up to 100 mmol Mo g^{-1} ferrihydrite under similar environmental conditions. These authors showed that ferrihydrite transformation following the addition of 0.5 mM Fe(II) shifted the coordination of co-precipitated Mo(VI) from tetrahedral to octahedral. These findings are generally consistent with the current study, where both Fe(II)- and S(-II) driven ferrihydrite transformation corresponds to a shift from tetrahedral to octahedral Mo coordination and the formation of Mo-bearing FeOx phases and discrete Mo minerals.

The relatively low abundance (25 μmol Mo g^{-1}) of co-precipitated Mo(VI) may have favored reaction between S(-II) and structural Fe(III) at the ferrihydrite surface. Kraal et al. (2022) found that high surface loadings of adsorbed PO_4^{3-} concentrations limited $Fe(II)_{(aq)}$ uptake and inhibited extensive FeOx transformation via the ET-AE reaction. However, the absence of adsorbed MoO_4^{2-} in our experiments should favor $Fe(II)_{(aq)}$ and $S(-II)_{(aq)}$ uptake and ferrihydrite transformation. Low aqueous Mo concentrations persisted over the first 14 d of the S(-II) experiments, when extensive ferrihydrite transformation produced lepidocrocite, goethite, and minor amounts of elemental S and FeS. Limited changes in Mo coordination and bonding after 14 d suggests ongoing sulfidation and corresponding Mo-S bonding was thermodynamically or kinetically limited (Poulton et al., 2004).

This study examines repartitioning of co-precipitated Mo(VI) during redox-induced ferrihydrite transformation. Associated results differ from similar experiments where reactions between $Mo(VI)_{(aq)}$ and $S(-II)_{(aq)}$ produce different Mo sequestration pathways (Erickson and Helz, 2000; Scholz et al., 2017; Smedley and Kinniburgh, 2017). The precipitation of FeS is an important control on $Fe(II)_{(aq)}$ and $S(-II)_{(aq)}$ concentrations in many anaerobic environments. Limited FeS precipitation under Fe(II)-limited conditions could leave $S(-II)_{(aq)}$ available for thiomolybdate formation (Erickson and Helz, 2000). Previous work by Dahl and Wirth (2017) suggest the progressive Mo(VI) sulfidation toward tetrathiomolybdate (MoS_4^{2-}) when Fe minerals are limited or absent. However, our results suggest thiomolybdate formation is limited by Mo association with initial and neoformed phases during Fe(II) and S(-II) driven transformation of ferrihydrite and, potentially, related FeOx phases that are ubiquitous in soils and sediments.

5. CONCLUSIONS AND IMPLICATIONS

In this study, we examined the repartitioning of co-precipitated Mo(VI) among reaction products of Fe(II) and S(-II) driven ferrihydrite transformation. These reactions produced goethite [α-FeOOH], lepidocrocite [γ-FeOOH], and magnetite [Fe_3O_4] formation in the Fe(II) experiments, with elemental S [S_8] and minor FeS also produced in the S(-II) experiments. Ongoing reaction favored goethite precipitation, which was the principal transformation product in the Fe(II) and S(-II) experiments. Observed Mo-O and Mo-Fe coordination and bonding were consistent with extensive Mo sequestration by FeOx minerals; however, discrete Mo minerals were also detected. We attribute the apparent absence of Mo-S bonding to limited Mo release and extensive S(-II) uptake during ferrihydrite transformation in the S(-II) experiment. Consistent pathways of ferrihydrite transformation and co-precipitated Mo(VI) repartitioning

indicate that Fe(II) catalyzed the electron transfer-atom exchange in both the Fe(II) and S(-II) experiments, with ferrihydrite sulfidation producing $Fe(II)_{(aq)}$ to support this reaction in the S(-II) experiments.

Previous studies have suggested that Mo sequestration principally occurs in permanently stratified water bodies with long residence times, where reactions between dissolved Mo(VI) and S(-II) species promote precipitation reactions over decades to centuries (Glass et al., 2013; Yang et al., 2015). However, Mo co-precipitation with FeOx and subsequent Mo sequestration may also occur when Fe(II) enters oxic waters, such as in marine systems near shorelines and river deltas. Deltas and shorelines can empty large concentrations of dissolved Fe(II) from lands including peatlands and volcanic soils to the ocean, where this reduced Fe(II) oxygenates and precipitates as FeOx (Krachler and Krachler, 2021; Rapp et al., 2020). Molybdenum co-precipitation with FeOx may occur during the combination of oxygenation and the increase in pH associated with salt water. As these newly co-precipitated particles sink, they become exposed to varied reducing conditions, similar to those conditions presented in this study, presenting an opportunity for Mo(VI) reduction. Although sequestration pathways and mechanisms remain elusive in marine systems, the formation of (oxy)thiomolybdates, Mo(VI) reduction, and Mo(VI) scavenging by particulate matter have been proposed. Other work in Fe(II)-rich systems suggests that sequestration of Mo(VI) may occur within FeOx structures or within discrete Mo(VI) bearing minerals (Gomez et al., 2013; Schoepfer et al., 2021, 2020). Our results reveal both reduction of Mo(VI) to Mo(IV) and precipitation of Mo(VI) compounds as driven by Fe cycling, processes which limit the bioavailability of Mo(VI). Limited bioavailability of Mo through sequestration by solid phases has corresponding implications for plants, animals, microbes, as all require Mo to grow and survive. Similarly, Mo limitation by

mineral sequestration has implications for global biogeochemical cycling of C, N, and S, which rely on Mo-based enzymes to continue.

ACKNOWLEDGEMENTS

Funding was provided by the Natural Sciences and Engineering Research Council of Canada (NSERC) through a Discovery Grant (Grant No. RGPIN-2020-05172) held by MBJL. VAS is a Fellow in the NSERC CREATE to INSPIRE program. A portion of the research described in this paper was performed at the Canadian Light Source, which is supported by the Canada Foundation for Innovation, NSERC, the University of Saskatchewan, the Government of Saskatchewan, Western Economic Diversification Canada, the National Research Council Canada, and the Canadian Institutes of Health Research. We thank Dr. Jullieta Lum and Dr. Elliott Skierszkan for assistance with XAS data collection and Dr. Joel Reid for XRD data collection, along with the Canadian Museum of Nature (Ottawa, Canada), Museums Victoria (Melbourne, Australia), the National Museum of Scotland (Edinburgh, Scotland) and the University of Arizona (Tuscon, USA) for mineral specimen loans.

SUPPLEMENTARY MATERIAL

The Supplementary Material provides details on the results of the Ferrozine method analysis, Mo L_{III}-edge XANES E_0 analysis, and tables outlining the Mo K-edge EXAFS models for the control, Fe(II) and S(-II) experiments.

DECLARATION OF COMPETING INTEREST

The authors declare that they have no known competing financial interests or personal relationships that could have appeared to influence the work reported in this paper.

AUTHOR INFORMATION

ORCID

Valerie A. Schoepfer: 0000-0002-9582-9940

Matthew B.J. Lindsay: 0000-0001-9123-3261

Author Contributions

The manuscript was written through contributions of both authors. Both authors have given approval for the final version of the manuscript.

DATA AVAILABILITY

Datasets related to this article can be found at http://doi.org/10.20383/103.0579, hosted at the Federated Research Data Repository (Schoepfer and Lindsay, 2022).

REFERENCES

[dataset] Schoepfer, V.A., Lindsay, M.B.J., 2022. Repartitioning of co-precipitated Mo(VI) during Fe(II) and S(-II) driven ferrihydrite transformation: Datasets and Supplementary Materials, Federated Research Data Repository, v1, http://doi.org/10.20383/103.0579.

Arai, Y., 2010. X-ray Absorption Spectroscopic Investigation of Molybdenum Multinuclear Sorption Mechanism at the Goethite−Water Interface. Environ. Sci. Technol. 44, 8491–8496. https://doi.org/10.1021/es101270g

Ardakani, O.H., Chappaz, A., Sanei, H., Mayer, B., 2016. Effect of thermal maturity on remobilization of molybdenum in black shales. Earth and Planetary Science Letters 449, 311–320. https://doi.org/10.1016/j.epsl.2016.06.004

Barron, A.R., Wurzburger, N., Bellenger, J.P., Wright, S.J., Kraepiel, A.M.L., Hedin, L.O., 2009. Molybdenum limitation of asymbiotic nitrogen fixation in tropical forest soils. Nature Geosci 2, 42–45. https://doi.org/10.1038/ngeo366

Boland, D.D., Collins, R.N., Miller, C.J., Glover, C.J., Waite, T.D., 2014. Effect of Solution and Solid-Phase Conditions on the Fe(II)-Accelerated Transformation of Ferrihydrite to Lepidocrocite and Goethite. Environ. Sci. Technol. 48, 5477–5485. https://doi.org/10.1021/es4043275

Bolanz, R.M., Grauer, C., Cooper, R.E., Göttlicher, J., Steininger, R., Perry, S., Küsel, K., 2017. Incorporation of molybdenum(vi) in akaganéite (β-FeOOH) and the microbial reduction of Mo–akaganéite by Shewanella loihica PV-4. CrystEngComm 19, 6189–6198. https://doi.org/10.1039/C7CE01569K

Bostick, B.C., Fendorf, S., Helz, G.R., 2003. Differential Adsorption of Molybdate and Tetrathiomolybdate on Pyrite (FeS_2). Environ. Sci. Technol. 37, 285–291. https://doi.org/10.1021/es0257467

Burton, E.D., Johnston, S.G., Bush, R.T., 2011. Microbial sulfidogenesis in ferrihydrite-rich environments: Effects on iron mineralogy and arsenic mobility. Geochimica et Cosmochimica Acta 75, 3072–3087. https://doi.org/10.1016/j.gca.2011.03.001

Carlson, L., Bigham, J.M., Schwertmann, U., Kyek, A., Wagner, F., 2002. Scavenging of As from Acid Mine Drainage by Schwertmannite and Ferrihydrite: A Comparison with Synthetic Analogues. Environ. Sci. Technol. 36, 1712–1719. https://doi.org/10.1021/es0110271

Cesbron, F., Ginderow, D., 1985. La sidwillite, MoO3.2H2O ; une nouvelle espèce minérale de Lake Como, Colorado, U.S.A. bulmi 108, 813–823. https://doi.org/10.3406/bulmi.1985.7899

Chapman, B.M., Jones, D.R., Jung, R.F., 1983. Processes controlling metal ion attenuation in acid mine drainage streams. Geochimica et Cosmochimica Acta 47, 1957–1973. https://doi.org/10.1016/0016-7037(83)90213-2

Chappaz, A., Gobeil, C., Tessier, A., 2008. Geochemical and anthropogenic enrichments of Mo in sediments from perennially oxic and seasonally anoxic lakes in Eastern Canada. Geochimica et Cosmochimica Acta 72, 170–184. https://doi.org/doi:10.1016/j.gca.2007.10.014

Dahl, T.W., Canfield, D.E., Rosing, M.T., Frei, R.E., Gordon, G.W., Knoll, A.H., Anbar, A.D., 2011. Molybdenum evidence for expansive sulfidic water masses in ~750Ma oceans. Earth and Planetary Science Letters 311, 264–274. https://doi.org/10.1016/j.epsl.2011.09.016

Dahl, T.W., Chappaz, A., Fitts, J.P., Lyons, T.W., 2013. Molybdenum reduction in a sulfidic lake: Evidence from X-ray absorption fine-structure spectroscopy and implications for the Mo paleoproxy. Geochimica et Cosmochimica Acta 103, 213–231. https://doi.org/10.1016/j.gca.2012.10.058

Dahl, T.W., Chappaz, A., Hoek, J., McKenzie, C.J., Svane, S., Canfield, D.E., 2017. Evidence of molybdenum association with particulate organic matter under sulfidic conditions. Geobiology 15, 311–323. https://doi.org/10.1111/gbi.12220

Dahl, T.W., Wirth, S.B., 2017. Molybdenum isotope fractionation and speciation in a euxinic lake—Testing ways to discern isotope fractionation processes in a sulfidic setting. Chemical Geology 460, 84–92. http://dx.doi.org/10.1016/j.chemgeo.2017.04.018

Das, S., Essilfie-Dughan, J., Jim Hendry, M., 2016. Sequestration of molybdate during transformation of 2-line ferrihydrite under alkaline conditions. Applied Geochemistry 73, 70–80. https://doi.org/10.1016/j.apgeochem.2016.08.003

Demtröder, L., Narberhaus, F., Masepohl, B., 2019. Coordinated regulation of nitrogen fixation and molybdate transport by molybdenum: Molybdenum regulation of nitrogen fixation. Mol Microbiol 111, 17–30. https://doi.org/10.1111/mmi.14152

Endo, Y., Kanazawa, Y., Sasaki, A., 1986. External form of kamiokite crystal. Bulletin of the Geological Soceity of Japan 37, 367–371.

Erickson, B.E., Helz, G.R., 2000. Molybdenum(VI) speciation in sulfidic waters: Stability and lability of thiomolybdates 10.

Essilfie-Dughan, J., Pickering, I.J., Hendry, M.J., George, G.N., Kotzer, T., 2011. Molybdenum Speciation in Uranium Mine Tailings Using X-Ray Absorption Spectroscopy. Environ. Sci. Technol. 45, 455–460. https://doi.org/10.1021/es102954b

Fox, P.M., Doner, H.E., 2003. Accumulation, Release, and Solubility of Arsenic, Molybdenum, and Vanadium in Wetland Sediments. J. Environ. Qual. 32, 2428–2435. https://doi.org/10.2134/jeq2003.2428

Freitas, A.P., André, R.F., Poucin, C., Le, T.K.-C., Imbao, J., Lassalle-Kaiser, B., Carenco, S., 2021. Guidelines for the Molybdenum Oxidation State and Geometry from X-ray Absorption Spectroscopy at the Mo L $_{2,3}$ -Edges. J. Phys. Chem. C 125, 17761–17773. https://doi.org/10.1021/acs.jpcc.1c01875

Glass, J.B., Axler, R.P., Chandra, S., Goldman, C.R., 2012. Molybdenum limitation of microbial nitrogen assimilation in aquatic ecosystems and pure cultures. Front. Microbio. 3. https://doi.org/10.3389/fmicb.2012.00331

Glass, J.B., Chappaz, A., Eustis, B., Heyvaert, A.C., Waetjen, D.P., Hartnett, H.E., Anbar, A.D., 2013. Molybdenum geochemistry in a seasonally dysoxic Mo-limited lacustrine ecosystem. Geochimica et Cosmochimica Acta 114, 204–219. https://doi.org/10.1016/j.gca.2013.03.023

Goldberg, S., Chunming, S., Forster, H.S., 1998. Sorption of Molybdenum on Oxides, Clay Minerals, and Soils: Mechanisms and Models, in: Adsorption of Metals by Geomedia. Elsevier, pp. 401–426. https://doi.org/10.1016/B978-012384245-9/50020-7

Gomez, M.A., Jim Hendry, M., Hossain, A., Das, S., Elouatik, S., 2013. Abiotic reduction of 2-line ferrihydrite: effects on adsorbed arsenate, molybdate, and nickel. RSC Adv. 3, 25812. https://doi.org/10.1039/c3ra44769c

Görn, M.G., Bolanz, R.M., Parry, S., Göttlicher, J., Steininger, R., Majzlan, J., 2021. INCORPORATION OF Mo6+ IN FERRIHYDRITE, GOETHITE, AND HEMATITE. Clays Clay Miner. https://doi.org/10.1007/s42860-021-00116-x

Gupta, U.C., Lipsett, J., 1981. Molybdenum in Soils, Plants, and Animals, in: Advances in Agronomy. Elsevier, pp. 73–115. https://doi.org/10.1016/S0065-2113(08)60885-8

Gustafsson, J.P., 2003. Modelling molybdate and tungstate adsorption to ferrihydrite. Chemical Geology 200, 105–115. https://doi.org/10.1016/S0009-2541(03)00161-X

Gustafsson, J.P., Tiberg, C., 2015. Molybdenum binding to soil constituents in acid soils: An XAS and modelling study. Chemical Geology 417, 279–288. https://doi.org/10.1016/j.chemgeo.2015.10.016

Han, Y.-S., Park, J.-H., Kim, S.-J., Jeong, H.Y., Ahn, J.S., 2019. Redox transformation of soil minerals and arsenic in arsenic-contaminated soil under cycling redox conditions. Journal of Hazardous Materials 378, 120745. https://doi.org/10.1016/j.jhazmat.2019.120745

Hansel, C.M., Benner, S.G., Fendorf, S., 2005. Competing Fe(II)-Induced Mineralization Pathways of Ferrihydrite. Environ. Sci. Technol. 39, 7147–7153. https://doi.org/10.1021/es050666z

Helz, G.R., Bura-Nakić, E., Mikac, N., Ciglenečki, I., 2011. New model for molybdenum behavior in euxinic waters. Chemical Geology 284, 323–332. https://doi.org/10.1016/j.chemgeo.2011.03.012

Helz, G.R., Miller, C.V., Charnock, J.M., Mosselmans, J.F.W., Pattrick, R.A.D., Garner, C.D., Vaughan, D.J., 1996. Mechanism of molybdenum removal from the sea and its concentration in black shales: EXAFS evidence. Geochimica et Cosmochimica Acta 60, 3631–3642. https://doi.org/10.1016/0016-7037(96)00195-0

Helz, G.R., Vorlicek, T.P., 2019. Precipitation of molybdenum from euxinic waters and the role of organic matter. Chemical Geology 509, 178–193. https://doi.org/10.1016/j.chemgeo.2019.02.001

Helz, G.R., Vorlicek, T.P., Kahn, M.D., 2004. Molybdenum Scavenging by Iron Monosulfide. Environ. Sci. Technol. 38, 4263–4268. https://doi.org/10.1021/es034969+

Hockmann, K., Planer-Friedrich, B., Johnston, S.G., Peiffer, S., Burton, E.D., 2020. Antimony mobility in sulfidic systems: Coupling with sulfide-induced iron oxide transformations. Geochimica et Cosmochimica Acta 282, 276–296. https://doi.org/10.1016/j.gca.2020.05.024

Huang, F.-G., Jia, S.-Y., Liu, Y., Wu, S.-H., Han, X., 2015. Reductive dissolution of ferrihydrite with the release of As(V) in the presence of dissolved S(-II). Journal of Hazardous Materials 286, 291–297. https://doi.org/10.1016/j.jhazmat.2014.12.035

Hudson-Edwards, K.A., Schell, C., Macklin, M.G., 1999. Mineralogy and geochemistry of alluvium contaminated by metal mining in the Rio Tinto area, southwest Spain. Applied Geochemistry 14, 1015–1030. https://doi.org/10.1016/S0883-2927(99)00008-6

Hunter, K.A., Boyd, P.W., 2007. Iron-binding ligands and their role in the ocean biogeochemistry of iron. Environ. Chem. 4, 221. https://doi.org/10.1071/EN07012

Hutchings, A.M., Basu, A., Dickson, A.J., Turchyn, A.V., 2020. Molybdenum geochemistry in salt marsh pond sediments. Geochimica et Cosmochimica Acta 284, 75–91. https://doi.org/10.1016/j.gca.2020.06.014

Jambor, J.L., Dutrizac, J.E., 1998. Occurrence and Constitution of Natural and Synthetic Ferrihydrite, a Widespread Iron Oxyhydroxide. Chem. Rev. 98, 2549–2586. https://doi.org/10.1021/cr970105t

Johan, Z., Picot, P., 1986. Kamiokite, Fez Mo30a, a Tetravalent Molybdenum Oxide: New Data and Occurrences. TMPM Tschermaks Mineralogische und Petrographische Mitteilungen 35, 67–75.

Kaiser, B.N., Gridley, K.L., Ngaire Brady, J., Phillips, T., Tyerman, S.D., 2005. The Role of Molybdenum in Agricultural Plant Production. Annals of Botany 96, 745–754. https://doi.org/10.1093/aob/mci226

Kanazawa, Y., Sasaki, A., 1986. Structure of kamiokite. Acta Crystallogr C Cryst Struct Commun 42, 9–11. https://doi.org/10.1107/S0108270186097500

Kashiwabara, T., Takahashi, Y., Tanimizu, M., Usui, A., 2011. Molecular-scale mechanisms of distribution and isotopic fractionation of molybdenum between seawater and ferromanganese oxides. Geochimica et Cosmochimica Acta 75, 5762–5784. https://doi.org/10.1016/j.gca.2011.07.022

Kocar, B.D., Borch, T., Fendorf, S., 2010. Arsenic repartitioning during biogenic sulfidization and transformation of ferrihydrite. Geochimica et Cosmochimica Acta 74, 980–994. https://doi.org/10.1016/j.gca.2009.10.023

Kocar, B.D., Herbel, M.J., Tufano, K.J., Fendorf, S., 2006. Contrasting Effects of Dissimilatory Iron(III) and Arsenic(V) Reduction on Arsenic Retention and Transport. Environ. Sci. Technol. 40, 6715–6721. https://doi.org/10.1021/es061540k

Kraal, P., van Genuchten, C.M., Behrends, T., 2022. Phosphate coprecipitation affects reactivity of iron (oxyhydr)oxides towards dissolved iron and sulfide. Geochimica et Cosmochimica Acta 321, 311–328. https://doi.org/10.1016/j.gca.2021.12.032

Krachler, R., Krachler, R.F., 2021. Northern High-Latitude Organic Soils As a Vital Source of River-Borne Dissolved Iron to the Ocean. Environ. Sci. Technol. 55, 9672–9690. https://doi.org/10.1021/acs.est.1c01439

Lindsay, S.S., Baedecker, M.J., 1988. Determination of Aqueous Sulfide in Contaminated and Natural Water Using the Methylene Blue Method, in: Collins, A.G., Johnson, A.I. (Eds.), Ground-Water Contamination: Field Methods: A Symposium, ASTM Special Technical Publication. Presented at the Symposium on Field Methods for Ground-Water Contamination Studies and Their Standardization, ASTM, Philadelphia, PA, pp. 349–357.

Liu, H., Li, P., Zhu, M., Wei, Y., Sun, Y., 2007. Fe(II)-induced transformation from ferrihydrite to lepidocrocite and goethite. Journal of Solid State Chemistry 180, 2121–2128. https://doi.org/10.1016/j.jssc.2007.03.022

Liu, X., Millero, F.J., 2002. The solubility of iron in seawater. Marine Chemistry 77, 43–54. https://doi.org/10.1016/S0304-4203(01)00074-3

Maia, L.B., Moura, I., Moura, J.J.G., 2017. Molybdenum and Tungsten- Containing Enzymes: An Overview, in: RSC Metallobiology Series. Royal Society of Chemistry, p. 80.

Marks, J.A., Perakis, S.S., King, E.K., Pett-Ridge, J., 2015. Soil organic matter regulates molybdenum storage and mobility in forests. Biogeochemistry 125, 167–183. https://doi.org/10.1007/s10533-015-0121-4

Mendel, R.R., Kruse, T., 2012. Cell biology of molybdenum in plants and humans. Biochimica et Biophysica Acta (BBA) - Molecular Cell Research 1823, 1568–1579. https://doi.org/10.1016/j.bbamcr.2012.02.007

Park, J.H., Han, Y.-S., Ahn, J.S., 2016. Comparison of arsenic co-precipitation and adsorption by iron minerals and the mechanism of arsenic natural attenuation in a mine stream. Water Research 106, 295–303. https://doi.org/10.1016/j.watres.2016.10.006

Parkhurst, D., L., Appelo, C.A.J., 2013. Description of Input and Examples for PHREEQC Version 3—A Computer Program for Speciation, Batch-Reaction, One-Dimensional Transport, and Inverse Geochemical Calculations, Modeling Techniques. U.S. Geological Survey.

Pedersen, H.D., Postma, D., Jakobsen, R., 2006. Release of arsenic associated with the reduction and transformation of iron oxides. Geochimica et Cosmochimica Acta 70, 4116–4129. https://doi.org/10.1016/j.gca.2006.06.1370

Perakis, S.S., Pett-Ridge, J.C., Catricala, C.E., 2017. Nutrient feedbacks to soil heterotrophic nitrogen fixation in forests. Biogeochemistry 134, 41–55. https://doi.org/10.1007/s10533-017-0341-x

Poulton, S.W., Krom, M.D., Raiswell, R., 2004. A revised scheme for the reactivity of iron (oxyhydr)oxide minerals towards dissolved sulfide. Geochimica et Cosmochimica Acta 68, 3703–3715. https://doi.org/10.1016/j.gca.2004.03.012

Rapp, I., Schlosser, C., Browning, T.J., Wolf, F., Le Moigne, F.A.C., Gledhill, M., Achterberg, E.P., 2020. El Niño-Driven Oxygenation Impacts Peruvian Shelf Iron Supply to the South Pacific Ocean. Geophys. Res. Lett. 47. https://doi.org/10.1029/2019GL086631

Ravel, B., 2001. *ATOMS* : crystallography for the X-ray absorption spectroscopist. J Synchrotron Rad 8, 314–316. https://doi.org/10.1107/S090904950001493X

Ravel, B., Newville, M., 2005. *ATHENA* , *ARTEMIS* , *HEPHAESTUS* : data analysis for X-ray absorption spectroscopy using *IFEFFIT*. J Synchrotron Rad 12, 537–541. https://doi.org/10.1107/S0909049505012719

Robertson, J.M., Nesbitt, J.A., Lindsay, M.B.J., 2019. Aqueous- and solid-phase molybdenum geochemistry of oil sands fluid petroleum coke deposits, Alberta, Canada. Chemosphere 217, 715–723. https://doi.org/10.1016/j.chemosphere.2018.11.064

Rousk, K., Degboe, J., Michelsen, A., Bradley, R., Bellenger, J., 2017. Molybdenum and phosphorus limitation of moss-associated nitrogen fixation in boreal ecosystems. New Phytol 214, 97–107. https://doi.org/10.1111/nph.14331

Sasaki, A., Yui, S., Yamaguchi, M., 1985. Kamiokite, Fe2Mo3O8, a new mineral. Mineralogical Journal 12, 393–399. https://doi.org/10.2465/minerj.12.393

Schindelin, J., Arganda-Carreras, I., Frise, E., Kaynig, V., Longair, M., Pietzsch, T., Preibisch, S., Rueden, C., Saalfeld, S., Schmid, B., Tinevez, J.-Y., White, D.J., Hartenstein, V., Eliceiri, K., Tomancak, P., Cardona, A., 2012. Fiji: an open-source platform for biological-image analysis. Nat Methods 9, 676–682. https://doi.org/10.1038/nmeth.2019

Schoepfer, V.A., Lum, J.E., Lindsay, M.B.J., 2021. Molybdenum(VI) Sequestration Mechanisms During Iron(II)-Induced Ferrihydrite Transformation. ACS Earth Space Chem. acsearthspacechem.1c00152. https://doi.org/10.1021/acsearthspacechem.1c00152

Schoepfer, V.A., Qin, K., Robertson, J.M., Das, S., Lindsay, M.B.J., 2020. Structural Incorporation of Sorbed Molybdate during Iron(II)-Induced Transformation of Ferrihydrite and Goethite under Advective Flow Conditions. ACS Earth Space Chem. 4, 1114–1126. https://doi.org/10.1021/acsearthspacechem.0c00099

Scholz, F., McManus, J., Sommer, S., 2013. The manganese and iron shuttle in a modern euxinic basin and implications for molybdenum cycling at euxinic ocean margins. Chemical Geology 355, 56–68. https://doi.org/10.1016/j.chemgeo.2013.07.006

Scholz, F., Siebert, C., Dale, A.W., Frank, M., 2017. Intense molybdenum accumulation in sediments underneath a nitrogenous water column and implications for the reconstruction of paleo-redox conditions based on molybdenum isotopes. Geochimica et Cosmochimica Acta 213, 400–417. https://doi.org/10.1016/j.gca.2017.06.048

Schultz, M.F., Benjamin, M.M., Ferguson, J.F., 1987. Adsorption and desorption of metals on ferrihydrite: reversibility of the reaction and sorption properties of the regenerated solid. Environ. Sci. Technol. 21, 863–869. https://doi.org/10.1021/es00163a003

Schwarz, G., Mendel, R.R., Ribbe, M.W., 2009. Molybdenum cofactors, enzymes and pathways. Nature 460, 839–847. https://doi.org/10.1038/nature08302

Schwertmann, U., Cornell, R., 1991. Iron Oxides in the Laboratory, 2nd ed. Wiley, New York.

Skierszkan, E.K., Robertson, J.M., Lindsay, M.B.J., Stockwell, J.S., Dockrey, J.W., Das, S., Weis, D., Beckie, R.D., Mayer, K.U., 2019. Tracing Molybdenum Attenuation in Mining Environments Using Molybdenum Stable Isotopes. Environ. Sci. Technol. 53, 5678–5686. https://doi.org/10.1021/acs.est.9b00766

Smedley, P.L., Cooper, D.M., Ander, E.L., Milne, C.J., Lapworth, D.J., 2014. Occurrence of molybdenum in British surface water and groundwater: Distributions, controls and implications for water supply. Applied Geochemistry 40, 144–154. https://doi.org/10.1016/j.apgeochem.2013.03.014

Smedley, P.L., Kinniburgh, D.G., 2017. Molybdenum in natural waters: A review of occurrence, distributions and controls. Applied Geochemistry 84, 387–432. https://doi.org/10.1016/j.apgeochem.2017.05.008

Southall, S.C., Micklethwaite, S., Wilson, S.A., Frierdich, A.J., 2018. Changes in Crystallinity and Tracer-Isotope Distribution of Goethite during Fe(II)-Accelerated Recrystallization.

ACS Earth Space Chem. 2, 1271–1282. https://doi.org/10.1021/acsearthspacechem.8b00100

Swedo, K.B., Enemark, J.H., 1979. Some aspects of the bioinorganic chemistry of molybdenum. J. Chem. Educ. 56, 70. https://doi.org/10.1021/ed056p70

Tessin, A., Chappaz, A., Hendy, I., Sheldon, N., 2018. Molybdenum speciation as a paleo-redox proxy: A case study from Late Cretaceous Western Interior Seaway black shales. Geology 47. https://doi.org/10.1130/G45785.1

ThomasArrigo, L.K., Bouchet, S., Kaegi, R., Kretzschmar, R., 2020. Organic matter influences transformation products of ferrihydrite exposed to sulfide. Environ. Sci.: Nano 7, 3405–3418. https://doi.org/10.1039/D0EN00398K

Toby, B.H., Von Dreele, R.B., 2013. *GSAS-II* : the genesis of a modern open-source all purpose crystallography software package. J Appl Crystallogr 46, 544–549. https://doi.org/10.1107/S0021889813003531

Tomaszewski, E.J., Cronk, S.S., Gorski, C.A., Ginder-Vogel, M., 2016. The role of dissolved Fe(II) concentration in the mineralogical evolution of Fe (hydr)oxides during redox cycling. Chemical Geology 438, 163–170. https://doi.org/10.1016/j.chemgeo.2016.06.016

Usman, M., Hanna, K., Abdelmoula, M., Zegeye, A., Faure, P., Ruby, C., 2012. Formation of green rust via mineralogical transformation of ferric oxides (ferrihydrite, goethite and hematite). Applied Clay Science 64, 38–43. https://doi.org/10.1016/j.clay.2011.10.008

Viollier, E., Inglett, P.W., Hunter, K., Roychoudhury, A.N., Van Cappellen, P., 2000. The ferrozine method revisited: Fe(II)/Fe(III) determination in natural waters. Applied Geochemistry 15, 785–790. https://doi.org/10.1016/S0883-2927(99)00097-9

Vorlicek, T.P., Helz, G.R., Chappaz, A., Vue, P., Vezina, A., Hunter, W., 2018. Molybdenum Burial Mechanism in Sulfidic Sediments: Iron-Sulfide Pathway. ACS Earth Space Chem. 2, 565–576. https://doi.org/10.1021/acsearthspacechem.8b00016

Vorlicek, T.P., Kahn, M.D., Kasuya, Y., Helz, G.R., 2004. Capture of molybdenum in pyrite-forming sediments: role of ligand-induced reduction by polysulfides. Geochimica et Cosmochimica Acta 68, 547–556. https://doi.org/10.1016/S0016-7037(03)00444-7

Wagner, M., Chappaz, A., Lyons, T.W., 2017. Molybdenum speciation and burial pathway in weakly sulfidic environments: Insights from XAFS. Geochimica et Cosmochimica Acta 206, 18–29. https://doi.org/10.1016/j.gca.2017.02.018

Wang, D., Aller, R.C., Sañudo-Wilhelmy, S.A., 2011. Redox speciation and early diagenetic behavior of dissolved molybdenum in sulfidic muds. Marine Chemistry 125, 101–107. https://doi.org/10.1016/j.marchem.2011.03.002

Wichard, T., Mishra, B., Myneni, S.C.B., Bellenger, J.-P., Kraepiel, A.M.L., 2009. Storage and bioavailability of molybdenum in soils increased by organic matter complexation. Nature Geosci 2, 625–629. https://doi.org/10.1038/ngeo589

Williams, J.H., 1956. The effect of molybdenum on reclaimed Welsh upland pastures. Plant Soil 7, 327–340. https://doi.org/10.1007/BF01394321

Winbourne, J.B., Brewer, S.W., Houlton, B.Z., 2017. Iron controls over di-nitrogen fixation in karst tropical forest. Ecology 98, 773–781. https://doi.org/10.1002/ecy.1700

Wurzburger, N., Bellenger, J.P., Kraepiel, A.M.L., Hedin, L.O., 2012. Molybdenum and Phosphorus Interact to Constrain Asymbiotic Nitrogen Fixation in Tropical Forests. PLoS ONE 7, e33710. https://doi.org/10.1371/journal.pone.0033710

Xu, N., Braida, W., Christodoulatos, C., Chen, J., 2013. A Review of Molybdenum Adsorption in Soils/Bed Sediments: Speciation, Mechanism, and Model Applications. Soil and Sediment Contamination: An International Journal 22, 912–929. https://doi.org/10.1080/15320383.2013.770438

Xu, N., Christodoulatos, C., Braida, W., 2006. Adsorption of molybdate and tetrathiomolybdate onto pyrite and goethite: Effect of pH and competitive anions. Chemosphere 62, 1726–1735. https://doi.org/10.1016/j.chemosphere.2005.06.025

Yan, W., Zhou, J., Liu, H., Chen, R., Zhang, Y., Wei, Y., 2016. Formation of Goethite and Magnetite Rust via Reaction with Fe(II). Journal of The Electrochemical Society 8.

Yang, N., Welch, K.A., Mohajerin, T.J., Telfeyan, K., Chevis, D.A., Grimm, D.A., Lyons, W.B., White, C.D., Johannesson, K.H., 2015. Comparison of arsenic and molybdenum geochemistry in meromictic lakes of the McMurdo Dry Valleys, Antarctica: Implications for oxyanion-forming trace element behavior in permanently stratified lakes. Chemical Geology 404, 110–125. https://doi.org/10.1016/j.chemgeo.2015.03.029

Zhang, G., Yuan, Z., Lei, L., Lin, J., Wang, X., Wang, S., Jia, Y., 2019. Arsenic redistribution and transformation during Fe(II)-catalyzed recrystallization of As-adsorbed ferrihydrite under anaerobic conditions. Chemical Geology 525, 380–389. https://doi.org/10.1016/j.chemgeo.2019.08.002

Zheng, Y., Anderson, R.F., van Geen, A., Kuwabara, J., 2000. Authigenic molybdenum formation in marine sediments: a link to pore water sulfide in the Santa Barbara Basin. Geochimica et Cosmochimica Acta 64, 4165–4178. https://doi.org/10.1016/S0016-7037(00)00495-6

Graphical Abstract